Modelling of mixture preparation in a small engine with Port Fuel Injection

T.N.C. Anand* and R.V. Ravikrishna

Department of Mechanical Engineering,
Indian Institute of Science, Bangalore 560012, India
E-mail: anand@iitm.ac.in
E-mail: ravikris@mecheng.iisc.ernet.in
*Corresponding author

Abstract: Computational Fluid Dynamics simulations are performed to study mixture preparation in the intake manifold of a small engine with Port Fuel Injection. Data from laser-based experiments on two injectors are used as inputs to the spray sub-model. The results reveal improved in-cylinder fuel distribution when the spray is directed onto the intake valve. The Sauter Mean Diameter of the spray is observed to have an insignificant effect during open valve injection, while the targeting is found to have a large influence. The methodology developed as part of this work can be used to further optimize injection parameters in such engines.

Keywords: CFD; small engines; spray modelling; PFI; port fuel injection; spray characterisation; two-phase flow; mixture preparation.

Reference to this paper should be made as follows: Anand, T.N.C. and Ravikrishna, R.V. (xxxx) 'Modelling of mixture preparation in a small engine with Port Fuel Injection', *Progress in Computational Fluid Dynamics*, Vol. x, No. x, pp.xxx–xxx.

Biographical notes: T.N.C. Anand is an Assistant Professor at the Department of Mechanical Engineering at the Indian Institute of Technology Madras, Chennai, India. He received his PhD from the Indian Institute of Science, India in 2009. His research involves laser-based diagnostics and simulations of sprays and IC engine processes.

R.V. Ravikrishna is an Associate Professor in the Department of Mechanical Engineering at the Indian Institute of Science, Bangalore, India. He obtained his PhD from the School of Mechanical Engineering at Purdue University, USA. His research involves application of laser diagnostics in fluid dynamics and combustion research and numerical simulations.

1 Introduction

Over the last few years, stringent emission norms have been technology drivers for developments in Internal Combustion (IC) engines. Particularly with respect to small two-wheeler engines, emission norms in India are among the most stringent in the world, with limits of 1 g/km for CO emissions and 1 g/km for HC + NO_x emissions. However, while multi-cylinder engines have been well studied, modelling of manifold processes, specifically for small engines (less than 200 cc), has not received much attention in the literature. Some of the challenges specific to incorporating fuel injection strategies in small engines include higher maximum operating engine speed, packaging constraints, smaller bore size, electrical current consumption of the system, cost constraints and technology transfer to dealers and service people who are used to dealing with carburetted engines (Cathcart et al., 2004). The present work focuses on the mixture preparation in the intake manifold of a small 4-stroke engine with Port Fuel Injection (PFI).

The performance of PFI engines depends on a number of parameters related to the injection system itself. Hence, the PFI sub-system also needs to be tailored to the specific engine to obtain a robust performance of that engine under various operating conditions (Zhao et al., 1996). Computational Fluid Dynamics (CFD) simulations of port fuel injected engines can help in studying the effect of various parameters on engine performance. While CFD can reduce the cost of the design process, the insights provided by CFD in understanding the results from experiments are also extremely valuable, especially with respect to fine-tuning strategies for meeting future emission norms.

The present study uses a combination of theory and experiment wherein measurements of spray structure and droplet diameters are used as inputs for the CFD model. There have been only a few previous studies adopting a similar approach for small PFI engines, as discussed below. Murakami et al. (2004) used CFD as a tool to study the combustion phenomena in a 50 cc engine. The spray was simulated using the Lagrangian-Eulerian method, with the Taylor Analogy Breakup (TAB) model for secondary

breakup and experimental data to initialise the spray. The spray penetration and spray shape were matched and the model was used to study combustion. The authors observed that HC emissions reduced as the spray target angle increased (a higher angle indicates that the fuel is directed towards the throttle plate) due to reduced short-circuit losses. Short-circuit losses refer to the passage of fuel from the intake valve into the engine and out of the exhaust valve without combustion, and occur because of both valves being open (valve overlap) at the beginning of the intake process.

In a similar study on the effect of injection timing and targeting in a 4-valve motorcycle engine under idling conditions with a 3-hole and 4-hole injector, Bianchi et al. (2007) observed that for closed valve injection, advancing the injection leads to most of the fuel being vaporised. Closed-valve injection refers to injection of fuel into the manifold when the intake valve is closed, as opposed to open-valve injection, where the fuel is injected when the intake valve is open. Thus, there is a greater delay between the time of injection and the intake process in closed-valve injection.

In studies on the influence of parameters on combustion stability of small engines, air-blast type injectors with smaller SMD were found to give good combustion stability and small wall films (Kato et al., 2007). SMDs for an air-assisted M-jet low-pressure injector were found to be 120 micron without air assist, and 10 micron with air assist (Ishii et al., 2004), though details about the location of the measurements are not available.

General studies on PFI include those by Lenz (1992) who reviewed the spray characteristics of various injectors. Typical SMDs were reported to be in the range of 200 µm for multi-hole-type injectors and 300 µm for single-hole-type injectors. Kim et al. (2000) studied the measurement of spray angles of PFI injectors by different methods and observed that the definition and measurement of the spray angle is difficult due to the curved boundaries of the spray caused by air interaction. The spray angle was found to vary both with time and with axial distance from the injector tip, and with the technique used. Zhao et al. (1995) reviewed published literature on PFI and discussed the various types of PFI injectors and their resultant spray structures. The various stages of mixture formation were described, and the important parameters which affect vaporisation and transport processes, namely, fuel properties, injection duration, timing of the injection pulse with respect to the intake valve opening, spray pattern, droplet size distribution, intake port and valve temperatures, targeting accuracy and manifold pressure, were identified.

Unlike in small engines where the lack of space makes in situ visualisation and characterisation of the spray extremely difficult, large engines lend themselves easier for diagnostic studies. Arcoumanis et al. (1998) and Gold et al. (2000) experimentally studied flow under closed-valve and open-valve injection in a low speed 4-valve optical engine using laser-based techniques, and concluded that open-valve injection with a high tumble in the cylinder could lead to stable and efficient operation of the engine even at an air/fuel ratio of 24, through stratification. High speed visualisation of the fuelling process in the port of a 4-valve firing PFI engine under closed-valve injections were performed by Shin et al. (1995) who found the wall film flow to play an important role in fuel transport. Flow visualisation studies in the intake port of two 4-valve engines fitted with different injectors were performed by Zhao et al. (1996). The authors observed that while single stream injectors have good targeting, they have poor fuel dispersing characteristics. Hence, port geometry needs to be taken into account while choosing an injector. Different mechanisms of liquid fuel transport into the cylinder were identified by Meyer and Heywood (1997). The effects of various engine and fuel variables on liquid fuel transport into the cylinder were also studied by Meyer and Heywood (1999). Using Phase Doppler Particle Analyser (PDPA) measurements of the spray in a square piston optical engine with a flat cylinder head, the size of droplets entering the cylinder under open-valve injection was found to be smaller than that under closed-valve injection.

In summary, though the application of PFI to large engines has been well studied, only a few recent works have included experiments or CFD simulations on small PFI engines. Except for a few studies (Murakami et al., 2004; Ishii et al., 2004), little mention is found in the literature of engines of a capacity of 200 cc or less. Further, while CFD simulations of PFI engines can give insights and help optimise injection parameters such as injection timing, the results are only as good as the data which is input, and accurate initial and boundary conditions are critical to the reliability of the simulations. The transient and varying nature of low pressure sprays, and the absence of any satisfactory breakup models for this class of sprays, necessitates good experimental data. The present study includes characterisation of the spray from PFI injectors, and modelling of the two-phase flow in the intake manifold and cylinder of a four-stroke, single-cylinder, spark-ignited, two-wheeler engine, with fuelling done by a low-pressure port fuel injector. The uniqueness of the present study is that not only spatial, but temporal evolution of the spray from experiments has been studied in the CFD model for small engines. The present study considers conditions such as full load and part load at 3000 rpm.

2 Methodology

Laser-based diagnostic experiments were performed to characterise the unsteady spray from a two-hole and a four-hole injector under quiescent conditions. The spray structure, droplet sizes, SMD and velocities of the droplets were determined using techniques such as backlit imaging, Mie scattering, particle tracking velocimetry and Laser Sheet Drop (LSD) sizing. CFD simulations were then performed using the AVL FIRE software. Three-dimensional compressible, turbulent, multi-phase simulations of the flow both in the inlet manifold and the

in-cylinder region of the PFI engine were performed. The piston and valve motions were taken into account, and sub-models were used to model processes such as secondary break-up, wall film interaction, etc. The approach adopted involved feeding experimental values to the code wherever available, to improve the quality of the simulations and the level of confidence in the results. Specifically, since the spray model is the most complex, involving several assumptions and empirical constants, experimental values from the detailed laser-based experiments were used as inputs to the spray model.

2.1 Experimental characterisation of the injector

Experiments were performed on a low pressure PFI experimental facility, a schematic of which is shown in Figure 1. Only a brief description of the setup and results is presented here, as a more detailed description is available in Anand et al. (2010). The setup consists of a low-pressure pump and fuel tank coupled with the PFI injector. Control over the injection duration and injection frequency was achieved by using a function generator. An Nd:YAG laser with appropriate optics was used to illuminate the spray. A delay generator was used to change the time at which images could be acquired after the start of the spray. Images were acquired using CCD cameras connected to computers. Two low-pressure injectors were tested. The quantities measured and the techniques which were used to measure them are tabulated in Table 1. The nozzle hole diameters of the injectors were determined from microscope images, and were found to be 270 µm and 190 µm respectively for the 2-hole and 4-hole injectors, while the mass injected was found to be 12 mg per 8 ms electronic pulse. A schematic of the nozzle exit plane is shown in Figure 2. Since the mass flow rate could not be measured directly, the shape of the curve was assumed from the needle lift curve for voltage controlled injectors given by Lenz (1992), with the area fitted to give the total mass injected, as shown in Figure 3. The difference between the electronic and hydraulic time was determined from the experiments and also taken into account in simulations.

Figure 1 Schematic of the experimental setup

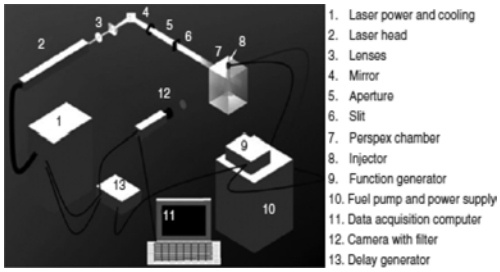

Source: Anand et al. (2010)

Figure 2 Schematic showing the bottom plate of the 2-hole (left) and 4-hole (right) injectors

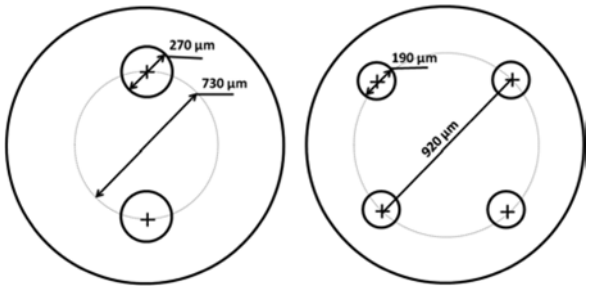

Experiments were performed on the low pressure PFI experimental facility described earlier. The injection pressure was maintained at 2.4 bar (gauge pressure) and the fuel was sprayed into the ambient (0.9 bar absolute). Mie scattering and backlit images of the spray were taken with an Nd:YAG laser and CCD cameras. Figure 4 shows backlit images of the spray taken with backlighting provided by the laser and fluorescent plates. Since this is a low-pressure spray, the backlit image shows the presence of large ligaments close to the injector. Information on the presence of ligaments is especially useful, since it helps identify the domain where droplet sizing will work – most common techniques assume that particles are spherical, which is not a valid assumption in the presence of ligaments.

Figure 3 Variation of mass flow rate of fuel with time as used in the simulations

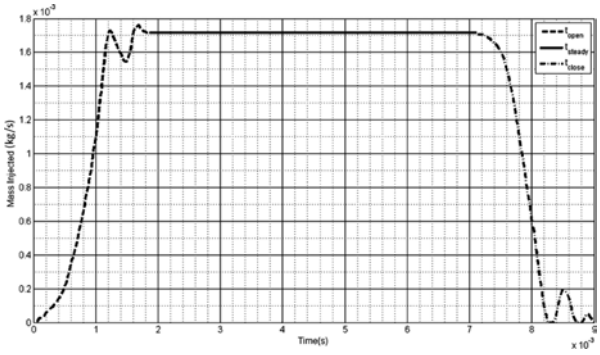

Table 1 Properties measured and the techniques adopted

Property	*Technique*
Nozzle hole diameter	Microscopy
Total mass injected	Mass balance
Mass flow rate	Curve fit with measured velocity
Spray cone angle	Mie scattering
Spray tip penetration	Mie scattering
Droplet sizes and distribution	Granulometry
Injection velocity	Particle tracking velocimetry

Figure 4 Backlit image of the spray at 5.5 ms after the start of injection, and close-up image of the near nozzle region

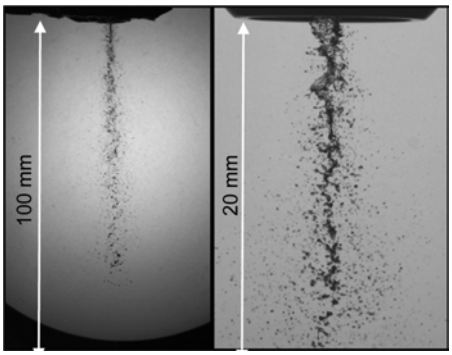

Droplet diameters in the spray were determined by taking close-up images of the Mie scattering in a 1 cm by 1.3 cm region (1036×1360 pixels of 9 µm size) in the mid-plane of the spray, and counting the pixels forming each drop in the image. This granulometry procedure was repeated for sets of 300 images taken at 2 ms intervals of time after the start of injection. Using this data, the SMDs of the spray were determined at different locations from the nozzle tip, at 2 ms intervals of time. The variations of SMD with time for the 2-hole injector, at an axial location 45 mm from the injector, are shown in Figure 5. It is observed that the SMD is initially high, followed by a nearly constant region. This is followed by a low SMD.

Figure 5 Variation of the SMD of the spray with time at a location 45 mm from the injector tip

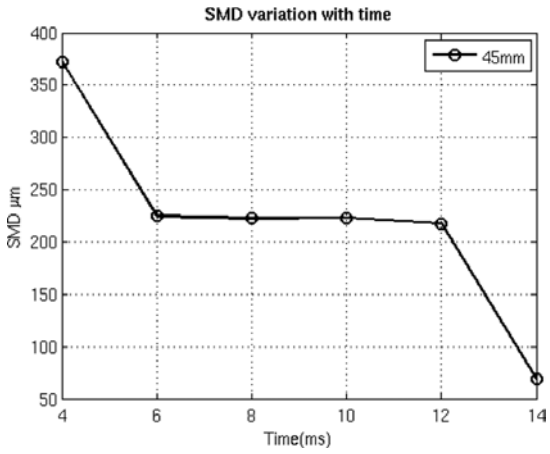

At the section 45 mm from the tip of the nozzle, the SMD drops sharply from 364 µm at 4 ms to 220 µm at 6 ms, after which it remains fairly constant till 12 ms. Since injection is a transient event, the Reynolds number of injection varies from 0 to a value of about 9000, and then decreases again. The initial high value is probably due to the injection of large droplets at the start of injection. During the bulk of the injection, the injection rate and hence, the SMD remain constant. Later, while the injection tapers off around 12 ms, the SMD also drops. This could be due to the fact that while the larger droplets fall rapidly, the smaller droplets drift in the air longer, leading to a smaller SMD. A similar trend is observed at axial locations, 70 mm and 100 mm from the injector, with the SMD being high initially and then falling. Results for the 4-hole injector are similar to those obtained for the 2-hole injector. The SMD of the spray from the 4-hole injector is, however, lower at around 120 micron.

Droplet distributions were also obtained at these axial locations as a function of time, a sample of which is shown in Figure 6. Particle-tracking velocimetry was also performed on images taken with a double pulsed Nd:YAG laser and PIV camera, and the velocity of the droplets near the injector tip was found to be 21 m/s.

Thus, a comprehensive study of the spray was done with state-of-the-art techniques, with all the important parameters such as the spray angle, spray tip penetration, mass injected, droplet velocities, droplet distributions and SMDs being measured. More importantly, information on the spatial and temporal evolution of the spray was generated.

Figure 6 Droplet distribution at 45 mm from the injector tip at 4ms after the start of injection (see online version for colours)

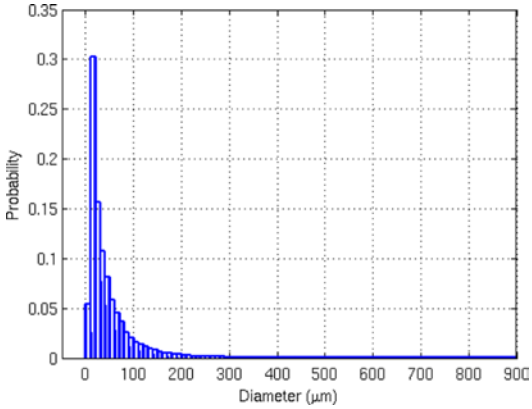

2.2 CFD details

Three-dimensional, two-phase, compressible flow CFD simulations were performed using the AVL FIRE software. Favre-averaged equations were solved, with the equation for a general variable being of the form:

$$\frac{\partial(\rho\phi)}{\partial t}+\frac{\partial}{\partial x_k}(\rho(U_k-U_{bk})\phi)=\frac{\partial}{\partial x_k}\left(\Gamma_\phi^{kk}\frac{\partial\phi}{\partial x_k}\right)+S_\phi \qquad (1)$$

where, ρ is the density of the fluid, φ is a general variable and Γ is the corresponding diffusivity, S_φ represents the source term, $U_k\,(k=1, 2, 3)$ represents the velocity components, and U_{bk} are the components of velocity of the moving boundary of the control volume. The values of these terms for the continuity, momentum, turbulent kinetic energy, enthaply and species conservation equations are listed in Table 2, along with the values of the various constants used (AVL List GmbH, 2008). A standard high-Reynold's number turbulence model was used to model the turbulent kinetic energy and dissipation,

with standard wall functions in the near-wall regions. The two-phase flow was modelled in the Lagrangian-Eulerian method, with the gas phase modelled in an Eulerian way, and the liquid phase, which is the discrete phase, handled in a Lagrangian way. Two-way coupling of the source terms was used with the Eulerian phase affecting the droplets and vice versa.

The momentum equation for the liquid phase is given by

$$m_d \frac{du_{\mathrm{id}}}{\mathrm{d}t} = F_{\mathrm{idr}} + F_{\mathrm{ig}} + F_{\mathrm{ip}} + F_{\mathrm{ib}} \tag{2}$$

where, m_d is the droplet mass, and u_{id} is its velocity vector, F_{idr} is the drag force (the subscript '*i*' indicating vector quantities), F_{ig} is a force which takes into account gravity and buoyancy, F_{ip} is the pressure force, and F_{ib} takes into account any body forces (zero in the present calculations). The expressions for these forces are given below.

$$F_{\mathrm{idr}} = D_p \cdot u_{\mathrm{irel}} \tag{3}$$

where u_{irel} is the relative velocity with magnitude $|u_{\mathrm{rel}}|$, and D_p represents the drag which is given by

$$D_p = \frac{1}{2}\rho_g A_d C_D \left|u_{\mathrm{rel}}\right|. \tag{4}$$

Here, C_D is the drag coefficient and A_d is the projected area of the droplet. ρ represents the density, with the subscript g referring to the gas phase. The drag coefficient C_D varies with the droplet Reynold's number as

$$C_D = \begin{cases} \dfrac{24}{\mathrm{Re}_d}\left(1 + 0.15\,\mathrm{Re}_d^{0.687}\right) & \text{for } \mathrm{Re}_d \le 10^3 \\ 0.44 & \text{for } \mathrm{Re}_d > 10^3 \end{cases} \tag{5}$$

where, the Reynold's number is defined as

$$\mathrm{Re}_d = \frac{\rho_g \left|u_{\mathrm{rel}}\right| D_d}{\mu_g}. \tag{6}$$

Here, μ is the viscosity and D_d is the droplet diameter. The gravity and pressure forces are given by

$$F_{\mathrm{igr}} = V_d(\rho_d - \rho_g)g_i \tag{7}$$

$$F_{\mathrm{ip}} = V_d \nabla p \tag{8}$$

where V_d represents the volume of the particle.

Therefore, substituting the values of the various forces in equation (2), the final equation for the particle acceleration is given as

$$\frac{\mathrm{d}u_{\mathrm{id}}}{\mathrm{d}t} = \frac{3}{4} C_D \frac{\rho_g}{\rho_d}\left|u_{\mathrm{ig}} - u_{\mathrm{id}}\right|(u_{\mathrm{ig}} - u_{\mathrm{id}}) + \left(1 - \frac{\rho_g}{\rho_d}\right) g_i \tag{9}$$

which can be integrated over time to obtain the velocity of the droplet.

Table 2 Diffusion coefficients and source terms for different scalar equations

Equation	φ	*Diffusion coefficient* Γ^{kk}	*Source term* S_φ
Continuity	1	0	0
Momentum	U_i	$\mu_{\mathrm{eff}} = \mu + \mu_t$	$\dfrac{\partial}{\partial x_k}\left(\mu_{\mathrm{eff}}\dfrac{\partial U_k}{\partial x_i} - \delta_{ik}(2/3)\left(\mu_{\mathrm{eff}}\nabla\cdot\vec{U} + \rho k\right)\right) + \rho g_i$
Turbulent Kinetic Energy (TKE)	k	$\mu + \mu_t/\sigma_k$	$P + G - \varepsilon;\ P = 2\mu_t S_{ij}S_{ij} - \dfrac{2}{3}(\mu_t S_{kk} + k)S_{kk};\ G = -\dfrac{\mu_t}{\rho\sigma_\rho}\nabla\rho$
Dissipation of TKE	ε	$\mu + \mu_t/\sigma_\varepsilon$	$\left(C_{\varepsilon 1}P + C_{\varepsilon 3}G - C_{\varepsilon 4}k\dfrac{\partial U_k}{\partial x_k} - C_{\varepsilon 2}\varepsilon\right)\dfrac{\varepsilon}{k}$
Energy (total enthalpy)	H	$\lambda/C_P + \mu_t/Pr_t$	$\dfrac{\partial p}{\partial t} + \dfrac{\partial}{\partial x_k}\left(U_i\left[\tau_{ij} - \dfrac{2}{3}\rho k\delta_{ik} - \Gamma_H\dfrac{\partial U_i}{\partial x_k}\right]\right)$
Species	Y_i	$\rho D_i + \mu_t/\rho_{Yi}$	R

Values of constants: $\mu_t = C_\mu\rho\dfrac{k^2}{\varepsilon};\ C_\mu = 0.09;\ C_{\varepsilon 1} = 1.44;\ C_{\varepsilon 2} = 1.92;\ C_{\varepsilon 3} = 0.8;\ C_{\varepsilon 4} = 0.33;\ \sigma_k = 1;\ \sigma_\varepsilon = 1.3;\ \sigma_\rho = 0.9$

The heat and mass transfer processes during droplet evaporation are modelled by Dukowicz (1979) model, which assumes spherical symmetry of the droplet, the presence of a quasi-steady gas film around the droplet, uniform temperature within the droplet, and liquid-vapour thermal equilibrium on the droplet surface. Under these conditions, the rate of temperature change is determined by the energy balance. The energy transferred to a droplet either leads to an increase in its temperature or provides the latent heat of vaporisation:

$$m_d c_{pd}\frac{\mathrm{d}T_d}{\mathrm{d}t} = L\frac{\mathrm{d}m_d}{\mathrm{d}t} + \dot{Q} \tag{10}$$

where m_d is the mass of the droplet, T_d is its temperature, c_{pd} is the specific heat, and L is the latent heat. $\dot{Q}$ is the convective heat flux from the gas at temperature T_∞ to the droplet surface, and is given by

$$\dot{Q} = D_d\pi\lambda\mathrm{Nu}(T_\infty - T_d). \tag{11}$$

Here, Nu is the Nusselt number which is taken from the correlation of Ranz and Marshal as

$$\mathrm{Nu} = 2 + 0.6\,\mathrm{Re}_d^{1/2}\,\mathrm{Pr}^{1/3} \tag{12}$$

where Pr is the Prandtl number.

If the local surface heat flux is represented by $\dot{q}_s$ and the vapour mass flux is $\dot{f}_{vs}$, with the assumption of uniformity of the droplet surface conditions, the droplet energy equation reduces to

$$m_d c_{pd} \frac{\mathrm{d}T_d}{\mathrm{d}t} = \dot{Q}\left(1 + L\frac{\dot{f}_{vs}}{\dot{q}_s}\right). \tag{13}$$

While primary breakup was not modelled, the TAB model (O'Rourke and Amsden, 1987) was used to model secondary breakup of the droplets. In the TAB model, the droplet is assumed to be analogous to a spring mass system: the aerodynamic force on the droplet is the external force, the surface tension is represented by a spring force, and the viscosity can be modelled by the damping forces. The droplet is assumed to oscillate under the effect of these forces, with its acceleration given by:

$$\ddot{y} = \frac{C_F \rho_g u^2}{C_b \rho_l r^2} - \frac{C_k \sigma}{\rho_l r^3} y - \frac{C_d \mu_l}{\rho_l r^2}\dot{y}. \tag{14}$$

Here, y is the dimensionless displacement of the equator of the droplet from its equilibrium position, and u is the relative velocity between the gas and droplet. μ refers to the surface tension, and ρ is the density, with the subscripts l and g representing the liquid and gas phases, respectively. C_F, C_k, C_d, and C_b are model constants. The injected droplet oscillates normal to its injection direction, and when $y > 1$, the droplet breaks up into smaller droplets whose normal velocity is the same as that of the parent droplet. The SMD of the child droplets is determined from energy conservation, as below:

$$\frac{r}{r_{32}} = 1 + \frac{8\cdot K}{20} + \frac{\rho_l r^3}{\sigma}\dot{y}^2\left(\frac{6\cdot K - 5}{120}\right) \tag{15}$$

where r is the radius of the droplet, r_{32} is the Sauter mean radius, σ is the surface tension, and K is a constant. A Chi-square distribution is used to determine the actual sizes of the child droplets centred around the new SMD. In the present paper, results are reported for studies where the standard model constants of the TAB model have been utilised, as shown in Table 3.

Table 3 Details of spray and sub-models used

Parameter	*Value*
Mass of fuel injected	12 mg/cycle
Initial droplet diameter	Droplet distribution as shown in Figure 6
Droplet break-up model	TAB model with constants $C_k = 8$, $C_b = 0.5$, $C_d = 5$, $C_F = 0.3333$ (O'Rourke and Amsden, 1987)

Table 4 Details of spray and sub-models used (continued)

Parameter	*Value*
Turbulent dispersion model	Enable (turbulence correlation time from Gosman (1981) model)
Droplet evaporation	Dukowicz (1979)

The spray-wall interaction is taken into account using a Weber number-based model (Mundo et al., 1995, 1998), and a two-dimensional finite volume wall-film model with semi-empirical relations applicable for thin films (<500 μm). The interaction between the spray and the wall is assumed to be determined by the Reynold's and Ohnesorge numbers, which are given by the expressions:

$$\mathrm{Re}_D = \rho d_0 u_0/\mu \tag{16}$$

$$\mathrm{Oh} = \frac{\mu}{\sqrt{\rho\sigma d_0}}. \tag{17}$$

Here, the subscript 0 refers to the conditions before impact, d refers to the droplet diameter, and u refers to the normal velocity. A K-value is defined, which is a modified form of a Weber number, and is given by the expression

$$K = \mathrm{Oh}\cdot\mathrm{Re}_D^{1.25}. \tag{18}$$

This K-value determines the impingement regime. For K less than 57.7, the droplets are deposited completely at the wall without bouncing or breakup. In the splashing regime ($K > 57.7$), the droplets are partially shattered to produce a droplet size distribution for the reflected droplets. The ratio of the reflected to the impinging mass is given by

$$m_1/m_0 = 3.9869\cdot 10^{-21} K^{9.2133} \tag{19}$$

and the difference $m_0 - m_1$ is added to the film. The reflected drop sizes are also obtained from empirical correlations as

$$d_1/d_0 = 0.88 - 0.013K^{0.8}. \tag{20}$$

In the wall film model, the gas and liquid phases are treated as separate single phases with a coupling between the two phases. It is assumed that the film thickness is small compared to the gas flow diameter, and the film is parallel to the wall. Further, the inertial effects are assumed to be small compared to wall friction and interfacial shear stress. The model includes the effect of shear force, gravity, pressure gradient, evaporation, heat transfer, interaction with impinging sprays, and film entrainment into the main flow due to high shear forces.

2.3 Quiescent spray simulations

While single phase-flow modelling in CFD is at an advanced stage for the present class of flows, and the results of CFD are satisfactory, the same cannot be said of two-phase flow modelling. The breakup of low-pressure sprays is not very well understood, and none of the current

models is applicable directly to low-pressure sprays (Pierson et al., 2000). Hence, before using the CFD model to simulate the spray in the engine geometry, the spray was simulated in a quiescent chamber to match the experimental conditions, and validated. This approach is justified, since the spray is essentially injected into a quiescent region in the manifold after which it enters into the flow field in the manifold, as shown in Figure 7.

Figure 7 CAD model of the engine domain for PFI simulations

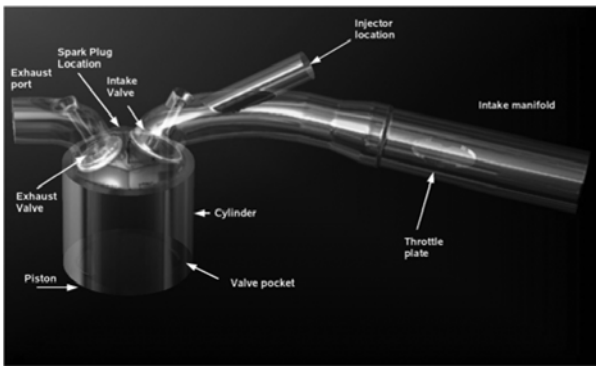

Figure 8 Comparison of the experimental and computed spray tip penetrations and SMD, with time

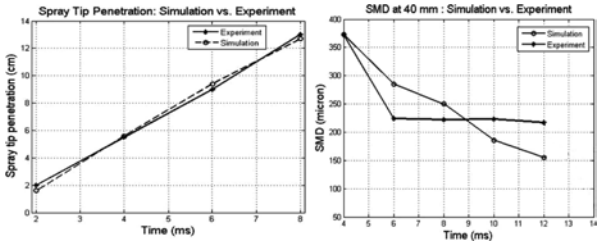

A computational domain 100×100 mm in cross section with a height of 200 mm was meshed, taking care to keep the mesh size the same as that in the spray region of the engine geometry. Wall boundaries were imposed on the sides of the chamber, with the nozzle positioned at the top. The mass of fuel injected was fixed at the experimental value of 1.2e-5 kg for all cases. The half-cone spray angle was input as 6° for the two-hole and four-hole injectors. The difference between the hydraulic and electronic injection times was also taken into account. Giving various input droplet diameters, and using various break-up models, it was found that none of them could satisfactorily predict the SMD and droplet distributions of the spray observed experimentally. Various input distributions were also tried, without much success. Finally, the droplet size distribution measured at 45 mm from the tip of the injector at 4 ms was input as the initial distribution at the injector location. With the injection curve used, the spray penetration could also be matched very well, as shown in Figure 8. With this input, it was found that the variation of SMD with time could be matched reasonably. It is observed that the match is very good at a time 4 ms after the start of injection, ut deviates later, with the maximum percentage difference in the SMD being in the range of around 25%. The coalescence-collision model was disabled, as suggested by Christ and Schlerfer (2000), as it predicted large changes in diameter which were not seen in the experimental results. Snapshots of the simulation results showing the spray structure, droplet sizes and velocities at 4 ms after the start of injection are shown in Figure 9.

Figure 9 CFD results for quiescent simulation: droplet positions and diameters (left)/velocities (right). The droplet sizes are proportional to the diameter, and the colour bars show the magnitudes of diameter (left)/velocity (right) (see online version for colours)

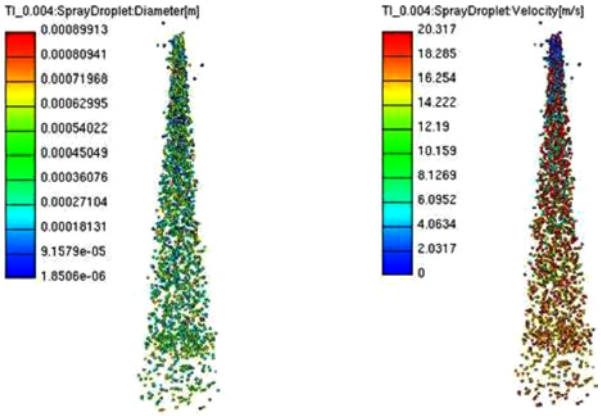

2.4 Engine and numerical grid details

The details of the engine simulated are mentioned in Table 4. The geometry is that of a small four-stroke, single-cylinder, air-cooled, 160 cc motorcycle engine. The geometrical details of the engine are shown in Figure 7. The geometry has been meshed with a FIRE Automated Meshing Engine (FAME) Engine Plus (FEP) mesh generator. The maximum cell size used in the current mesh is 1 mm, with refinements used at critical locations such as the valve and throttle gaps. Near the time of valve closure (valve lift of 0.3 mm), further refinement was done with cell sizes upto 0.125 mm. The total number of cells varies according to the domain, and the position of the piston. During the intake stroke, initially, the domain consists of the exhaust port, intake manifold and cylinder. Once the valve overlap period is over, the exhaust port is removed to reduce computational time. The domain then consists of the intake manifold and cylinder. After the intake stroke, the intake manifold is also removed, leaving only the cylinder where in-cylinder processes are simulated up to the compression Top Dead Centre (TDC). The total number of cells thus varies from around 200,000 to 1.4 million.

Table 5 Details of the engine simulated

Bore	62 mm
Stroke	52.9 mm
Compression ratio	9.4
Connecting rod length	108.3 mm

Table 6 Details of the engine simulated (continued)

Bore	62 mm
Fuel	Gasoline
Fuelling type	Port fuel injection
Stroke volume	159.7 cc
EVO	137° CA
IVO	337° CA
EVC	382° CA
IVC	597° CA
Simulation duration	383° CA for open valve injection

2.5 CFD simulations of engine

For the PFI engine simulations, static pressure values measured from experiments on a running engine were imposed at the inlet manifold boundary. The boundary location, and hence, the length of the intake manifold simulated were chosen such that the throttle plate was not too close to the boundary and matched the location where pressure taps could be located for the experiments. The values of pressure used are shown in Figure 10. The flow was driven by the cylinder whose displacement was in accordance with the velocity due to the crank angle, chosen speed, connecting rod length and stroke. Valve boundaries were also moving boundaries, with the displacements given by their respective valve timing diagrams. The conditions of the flow at the inlet were assumed to be fixed, with the turbulence length scale taken as half of the maximum inlet valve lift (7.1 mm at 470° CA), and the turbulence intensity assumed to be 10% of the mean flow velocity (Das and Dent, 1995). Thermal boundaries were applied as isothermal walls, with values chosen to be in the range of those found in Duclos and Zolver (1998), Selim et al. (1997), Wiedenhoefer and Reitz (2000) and AVL List GmbH (2008). The values of temperature applied at the various boundaries are tabulated in Table 5.

Figure 10 Plot showing the pressure boundary condition applied at the inlet (see online version for colours)

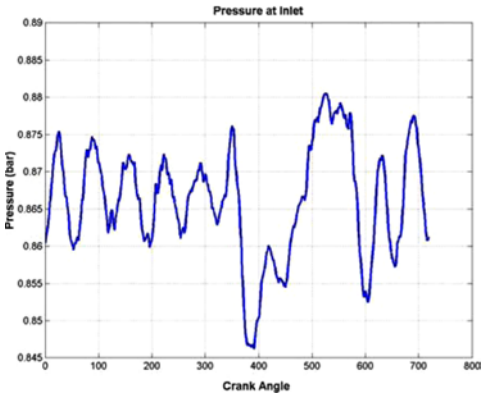

Table 7 Boundary conditions

Boundary	*Momentum boundary condition*	*Thermal boundary condition*
Inlet	Pressure = Time varying experimental value as per Figure 10	
	Turbulence intensity = 10% of mean velocity	300 K
	Turbulence length scale = 0.0035 m	
Intake manifold	Wall	300 K
Intake port	Wall	325 K
Head	Wall	500 K
Cylinder liner	Wall	450 K
Piston top	Wall with boundary velocity	450 K
Intake valve	Wall with boundary velocity	370 K
Exhaust valve	Wall with boundary velocity	450 K

Initial conditions were specified for the inlet manifold as ambient temperature, and mean pressure from the experimental data. The initial pressure in the cylinder was taken from experiments. An initial temperature of 750 K and an EGR mass fraction of 1 were specified in the cylinder and exhaust port to simulate burnt products at the inlet valve opening. The turbulent length scale in the cylinder was taken based on the clearance length (Heywood, 1998), and the turbulent kinetic energy and turbulence intensity were calculated using an expression from Heywood (1998):

$$\text{TKE} = (3/2)\times u'^2 \tag{21}$$

where u' is the turbulent fluctuation velocity given by:

$$u' = 2\times L\times n/60\times c. \tag{22}$$

The constant c which is suggested as 0.5 for normal automobile engines was modified to 0.7 to give a higher value of turbulence intensity, which is expected in small high-speed engines (AVL List GmbH, 2004).

2.6 Engine cases studied

Simulations of the PFI engine were conducted by varying the spray targeting angle, the injector, and the load. The simulation case for the spray from a 2-hole injector with the spray targeted at the back of the intake valve, and open-valve injection is referred to here as Case 1, or the baseline case. The details of the other cases which were studied are mentioned in Table 6.

Case 2 varies from the baseline case only in the injector orientation. Cases 3 and 4 are similar to the baseline case and Case 2, but employ a 4-hole injector. These cases are shown schematically in Figure 11. Case 5 involves studying the effect of heating the manifold wall, and finally, Case 6 is for a part-load condition.

Table 8 Details of the cases simulated. The parameters changed from the baseline case are italicised

Case	*Injection timing*	*Injector*	*Targeting*	*Wall temperature*	*Throttle position*	*Injection duration*	*Mass of fuel injected*
Case1	Open valve	2-hole	Intake valve	Normal	Full load	9 ms	1.21e-5 kg
Case2	Open valve	2-hole	*Manifold wall*	Normal	Full load	9 ms	1.21e-5 kg
Case3	Open valve	*4-hole*	Intake valve	Normal	Full load	9 ms	1.21e-5 kg
Case4	Open valve	*4-hole*	*Manifold wall*	Normal	Full load	9 ms	1.21e-5 kg
Case5	Open valve	2-hole	*Manifold wall*	*Heated*	Full load	9 ms	1.21e-5 kg
Case6	Open valve	2-hole	Intake valve	Normal	*Part load*	9 ms	1.21e-5 kg

Figure 11 Schematic showing the layout for cases 1–4

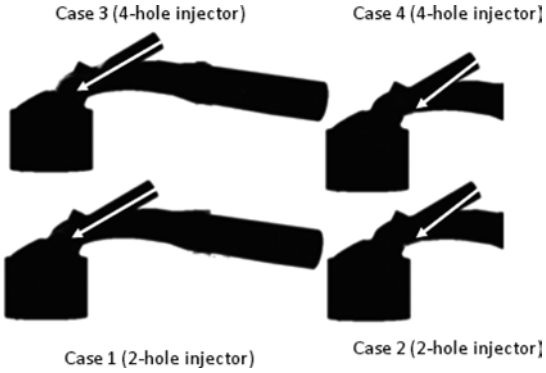

3 Results and discussion

The simulation begins at 337° CA with the opening of the intake valve. At this point of time, the exhaust valve is open, the blow down has completed and the pressure in the engine is less than the pressure in the intake manifold. Hence, there is no reverse flow into the intake manifold, and the fresh charge starts moving in immediately. Though the electronic injection pulse has been fed to the PFI injector, due to the injection delay, the fuel starts leaving the injector only at 341° CA. The fuel injected remains inside the passage connecting the injector with the manifold into which it is injected, and does not interact with air until much later. The same trend is seen at EVC (382° CA). At around 400° CA, the fuel enters the main airstream, and starts to interact with high velocity air. The following effects are observed: The air accelerates and deflects the smaller fuel droplets which now leave their original trajectory and follow the air flow, as seen in Figure 12, which shows velocity vectors in the mid-plane of the cylinder, and droplet positions and velocities. Many of the larger droplets break up on encountering the high velocity airstream. Due to deflection of the fuel spray, a large part of the spray does not impinge on the original targeted area on the intake valve. It is seen that most of the fuel flows over the intake valve and into the cylinder where some of it impinges on the cylinder liner and piston. Some droplets also get trapped in the valve pockets present in the piston. Since tumble is the dominant air flow pattern in this engine, the droplets also follow the tumble flow. Almost all of the droplets present, however, evaporate during the compression stroke, leaving a non-uniform distribution of fuel in the cylinder at spark timing (22° before TDC), as seen in Figure 13. The progression of the rich mixture into the cylinder is also seen here. At IVC, it is observed that some of the droplets, which were injected with a low velocity at the end of injection, still linger in the manifold, near the injector.

Figure 12 Velocity vectors in the mid-plane of the cylinder, and droplet positions for the baseline case at 450° CA. The colour bars show the magnitudes of air and droplet velocities (see online version for colours)

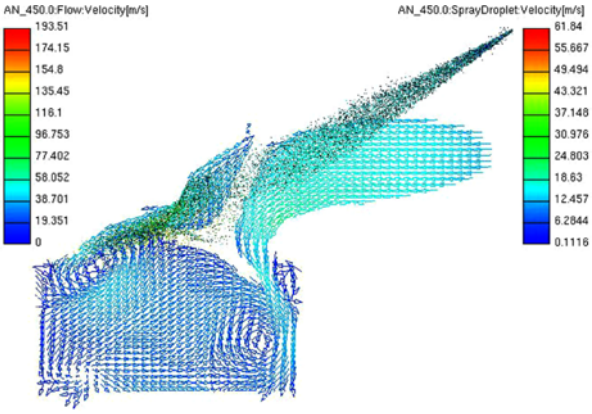

Figure 13 Fuel mass fractions in the mid-plane of the cylinder at 382°, 450°, 698°, and 597° CA (clockwise from top left). The colour bar shows the magnitude of fuel mass fraction (see online version for colours)

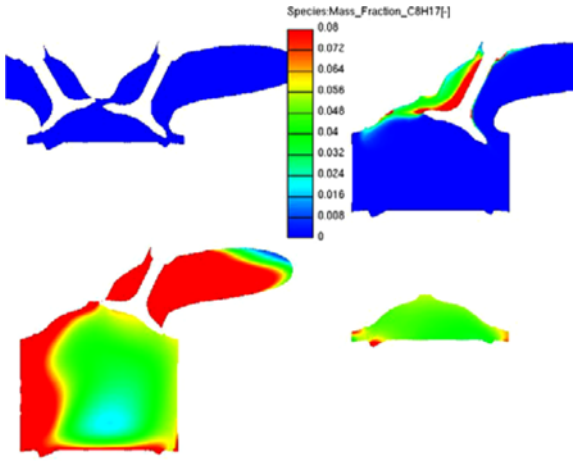

For open-valve injection, it is found that, as expected, both the 2-hole and 4-hole injectors give rise to a lower wall film mass in the intake manifold when the spray is injected at the intake valve (Cases 1 and 3). This is in agreement with the experimental findings of Meyer and Heywood (1999). When the spray is directed at the intake valve, the deflection of the spray is found to be higher due to the higher velocities in the near-valve region. The droplets get carried away by the high velocity intake flow into the cylinder, and less fuel is found to impinge on the valve. This is observed from Figure 14, which shows the variation of the wall film mass in the entire domain (cylinder + manifold region till IVC, only cylinder after IVC) with crank-angle. When the spray is directed at the manifold wall, however, a considerable portion of the spray still impinges on the manifold wall, though the spray is affected by the intake flow. Though the air stream has a considerable velocity under open-valve conditions, impingement is still found to occur. Therefore, the wall film mass in the manifold is higher. The wall film mass in the manifold does not vary much between Cases 2 and 4, where the spray is directed at the manifold walls from different injectors. However, there is a variation between Case 3 and the baseline case. The baseline case and Case 3 both have the spray directed to the back of the intake valve. Case 3 uses a 4-hole injector whose SMD is lower, and yet the wall film mass is higher. The reasons for this are as follows: though the spray is directed at the back of the inlet valve in both cases, the spray targeting is better for the 2-hole injector. Due to the lower SMD for the 4-hole injector, the deflection of the spray is higher – the smaller droplets tend to follow the air flow pattern more than in the previous case. Since most of the air enters the engine from above the inlet valve, the 4-hole injector tends to form wall films not only on the valve, but also on the upper side of the valve seat. The larger nozzle hole circle diameter for the 4-hole injector also means the spray is more spatially distributed, and this leads to impingement onto the walls of the passage connecting the nozzle and the inlet manifold, leading to larger films.

In Case 4, where the orientation of the 4-hole injector is changed, it is also observed that the targeting angle is not optimum for this injector. The higher spread from the 4-hole injector leads to the spray hitting the edge of the passage into which it is injected before emerging from it into the intake manifold. Thus, it is seen that the injector target angle needs to be fine-tuned for each injector specifically. The locations of the wall films and their thicknesses are shown in Figures 15 and 16.

It is often suggested that reducing the nozzle hole size, and hence the SMD of the spray, will be beneficial to engine performance. However, as observed here, the SMD of the spray together with other parameters such as the spread of the spray determines the presence of wall films. This has also been observed by Bianchi et al. (2007). Though the SMD is a very important parameter, as pointed out by Zhao et al. (1996), it is very important to select an injector specifically for a port geometry. Selecting an injector based on a smaller SMD alone can lead to adverse performance. Another observation in connection with the SMD is that the SMD of the droplets entering the cylinder is not significantly different in any of the open-valve cases. Meyer and Heywood (1999) explain that this is due to the high airstream velocity which breaks up the large droplets, leading to similar SMDs for injection onto both the intake valve and the intake manifold wall.

Figure 14 CFD results: comparison of mass of fuel wall film in the domain. The domain includes the cylinder and intake manifold till 597° CA, and only the cylinder beyond 597° CA

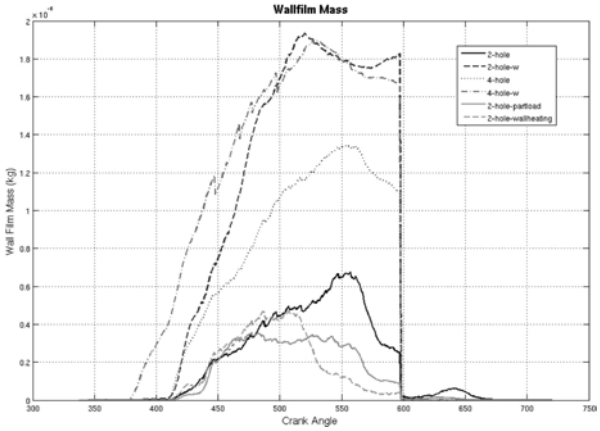

Figure 15 CFD results: front view of the domain showing the locations of wall films at IVC. Clockwise from left top: Case 3, Case 4, Case 2 and the Baseline case. The colour represents the thickness of the film (see online version for colours)

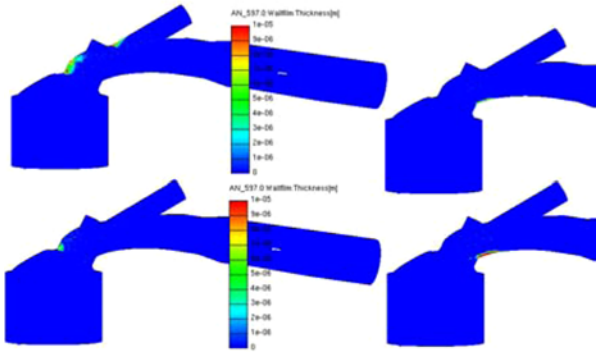

In line with the observations about the wall film masses discussed earlier, the mean mass fractions of fuel (Figure 17) in the cylinder show a similar trend. The mass fraction of fuel in the cylinder at the time of spark ignition is higher when the spray is directed onto the intake valve. When the spray is targeted at the intake valve, more of the fuel enters the cylinder where it evaporates. When the spray is directed at the manifold wall, however, some of the fuel does not directly enter and wall films are formed. The overall mass fraction of fuel in the cylinder is highest for the baseline case, and is lowest for Case 2. The 4-hole injectors (Cases 3 and 4) lie between these limits, with targeting at

the intake valve performing better than targeting at the manifold wall.

Figure 16 CFD results: top view of the domain showing the locations of wall films at IVC. Clockwise from left top: Case 3, Case 4, Case 2 and the Baseline case. The colour represents the thickness of the film (see online version for colours)

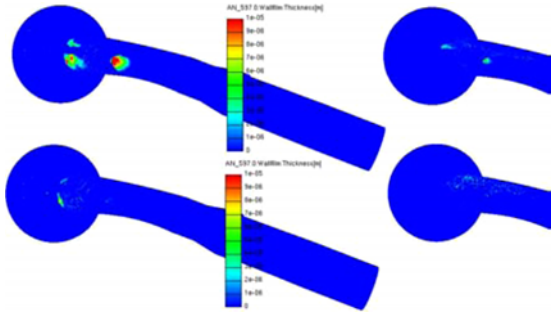

Figure 17 CFD results: comparison of mass fraction of fuel in the domain. The domain includes the cylinder and intake manifold till 597° CA, and only the cylinder beyond 597° CA (see online version for colours)

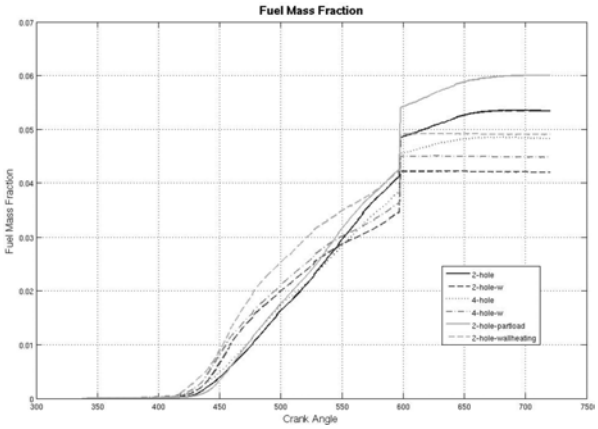

The contours of fuel mass fraction in the cylinder (Figures 18 and 19) reveal that complete mixing of the fuel does not take place in most cases. The intake of fuel vapour is also dependent on the injector targeting angle. In cases where the spray is targeted at the intake valve, the mass fraction of fuel is initially higher on the exhaust valve side as the fuel droplets flow over the intake valve. Later, this rich charge is carried down with the tumble motion. In all cases, the final charge inside the cylinder is lean, with the baseline case having the highest combustible charge close to the spark plug location at spark timing. Charge stratification is also observed from the simulation results when the spray is directed at the back of the intake valve, in agreement with earlier findings (Gold et al., 2000). The exact location of the rich region varies from case to case, and further studies may be required to ensure a rich mixture at the spark location under all operating conditions. However, the potential presence of stratification is very encouraging, as it can lead to an overall lean operation of the engine, leading to higher efficiencies.

In cases where the spray is directed at the manifold wall, a rich mixture is formed near it, upstream of the intake valve, and it flows into the cylinder below the inlet valve. However, due to the late intake valve closing, a large amount of rich charge once again flows out of the cylinder as the piston is moving up, and hence, the beneficial effect of the spray evaporating in the manifold is lost. Thus, the IVC time plays a very important role in determining the overall mass fraction of fuel in the cylinder under open-valve injection, with targeting onto the manifold wall. This is due to the fact that the wall films which are formed evaporate to some extent. Some of the droplets which do not enter the cylinder directly also evaporate, leading to a rich mixture in the manifold. Some of this mixture enters the cylinder below the intake valve towards the end of the intake stroke. However, the IVC timing determines if this charge remains within the cylinder or leaves the cylinder back into the manifold due to back flow from the cylinder at late IVC timings. Hence, the simulations suggest the need for variable valve timing.

Figure 18 CFD results: fuel mass fractions in the domain at inlet valve closure. Clockwise from left top: Case 3, Case 4, Case 2 and the Baseline case. The colour represents the magnitude of mass fraction (see online version for colours)

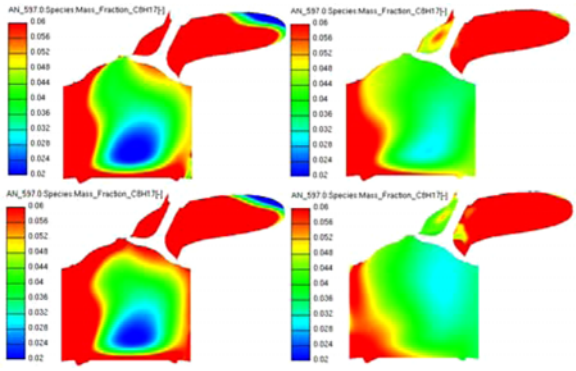

Figure 19 CFD results: fuel mass fractions in the spark plane of the cylinder at spark timing. Clockwise from left top: Case 3, Case 4, Case 2 and the Baseline case. The colour represents the magnitude of mass fraction (see online version for colours)

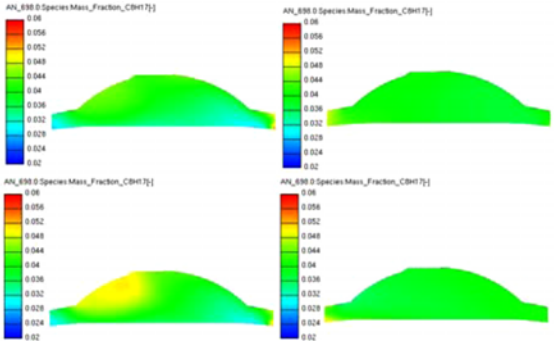

Earlier studies on large engines (Meyer and Heywood, 1999) have shown that the effect of heating the manifold

wall on the spray entering the cylinder is not significant when the spray is targeted at the intake valve. Therefore, the effect of wall heating has been studied here only where the fuel is targeted at the manifold wall. In Case 5 here, the port wall has been heated to 170°C. Though this temperature is rather high, this case is qualitatively indicative of the effects of wall heating, which could be to a lesser degree. Case 2 is the case which has the same parameters as Case 5, except for the port wall temperature. It is seen that Case 2 is also the case in which the wall film mass in the manifold is the highest among the cases studied. However, when the wall is heated, it is seen in Case 5 that the fuel film mass in the manifold reduces considerably, and is nearly negligible. This result is very encouraging, as a similar trend is likely to occur even with lower wall temperatures during closed-valve injection – as opposed to a high temperature available for a very short residence time; wall heating even at a lower temperature in that case would still have a much longer duration to evaporate any fuel film and improve fuelling.

In Case 5, as in Case 2, a large amount of fuel vapour is found to be present in the manifold, and some of it enters the cylinder below the intake valve. However, as observed earlier in Case 2, much of the rich charge is once again expelled from the cylinder just before IVC due to the late valve closing, as the piston is then moving up after reaching the bottom dead centre. Therefore, the full potential of the beneficial effect of wall heating is not reflected in the final mass fraction of fuel in the cylinder. However, it is likely to be seen at higher speeds where the ramming effect is likely to ensure minimal back flow before IVC.

Part-load throttle conditions for the baseline case have been studied in Case 6. Here, the injection duration has been maintained the same as in the baseline case, as the duration could not be determined experimentally. However, the throttle plate is inclined to the horizontal and pressure data corresponding to the part load case have been prescribed at the inlet boundary. Hence, the charge in the cylinder is expected to be on the richer side. It is observed that wall films are not significant under this condition. This suggests that the change in the flow field due to the change in inclination of the throttle plate has affected the flow field beneficially with respect to fuel impingement.

Consequently, most of the charge has entered the cylinder, and the mass fraction of the charge in the cylinder agrees with this. Figure 20 shows the mass fraction of fuel in the domain just before IVC. It is seen that much of the cylinder is filled with either near-stoichiometric or rich charge, though some locations are observed to have a lean mixture. The same trend is observed later also. At spark timing, the central plane has a near uniform mass fraction, but the spark plane shows the presence of stratification, with rich mixture present near the spark plug and lean mixture present near the piston.

Figure 20 CFD results: fuel mass fractions in the spark plane of the cylinder at spark timing. The colour represents the value of mass fraction (see online version for colours)

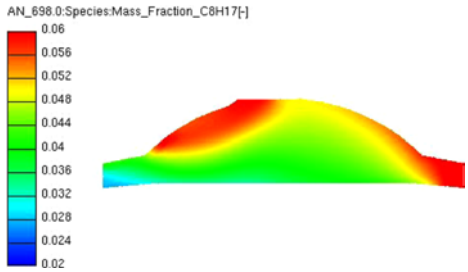

Figures 21 and 22 show three-dimensional lines which are loosely analogous to streamlines in two-dimensional space. The positions of droplets and the velocity in a plane close to the throttle plate are also shown. The differences in the flow fields between the baseline case (Figure 21) and the part-load case (Figure 22) are clearly visible – while most of the air flows smoothly in the baseline case, the throttle plate acts as a bluff body due to its inclination in Case 6. Hence, vortices are formed downstream of the plate, affecting the flow field greatly. The throttle plate also deflects a large portion of the flow. The spray is found to be positively affected by this field, with the impingement being lower, leading to less film mass.

Figure 21 CFD results: front view of the domain showing the directions of velocity, droplet positions and velocity magnitudes close to the throttle plate for the baseline case. The colour represents the magnitude of air/droplet velocity (see online version for colours)

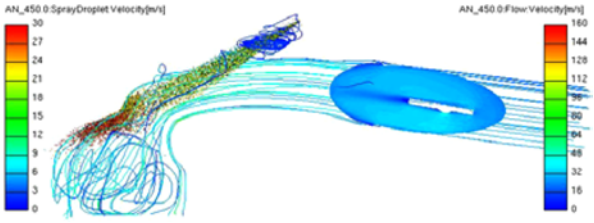

Figure 22 CFD results: front view of the domain showing the directions of velocity, droplet positions and velocity magnitudes close to the throttle plate for Case 6. The colour represents the magnitude of air/droplet velocity (see online version for colours)

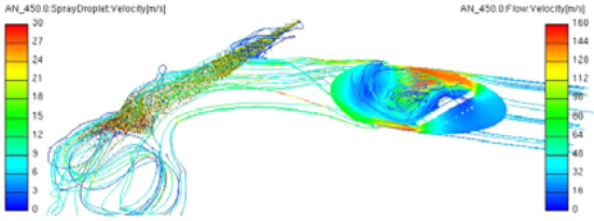

4 Conclusions

An approach of utilising experimental spray data in a CFD model has been used here for studying the effect of injection

parameters on PFI in small engines. It is observed from the simulations that the 4-hole injector forms thicker films than the 2-hole injector and the in-cylinder mass fraction of fuel is higher for the 2-hole injector. Thus, it is seen that an injector with a low SMD is not necessarily better under open-valve injection, as this can lead to poor targeting. The wall film mass is found to be lower when the spray is directed at the inlet valve than when it is directed onto the manifold wall. The mass fraction of fuel in the cylinder at the time of spark ignition is higher when the spray is directed onto the intake valve. However, the SMD of the droplets entering the cylinder is not significantly different in any of the open valve cases. IVC time plays a very important role in determining the overall mass fraction of fuel in the cylinder under open-valve injection targeted onto the manifold wall, and heating the wall leads to lower film thickness. Charge stratification is also observed in the cylinder at the time of spark ignition for some of the cases. In conclusion, the present simulations provide design inputs which can help in selecting a PFI injector for small engines, help in optimising the timing and injector target angle, and show potential for strategies such as manifold heating to reduce emissions in small engines.

References

Anand, T.N.C., Deshmukh, D., Madan Mohan, A. and Ravikrishna, R.V. (2010) 'Laser-based spatio-temporal characterisation of Port Fuel Injection (PFI) sprays', *International Journal of Spray and Combustion Dynamics*, Vol. 2, No. 2, pp.125–150.

Arcoumanis, C., Gold, M.R., Whitelaw, J.H., Xu, H.M., Gaade, J. and Wallace, S. (1998) *Droplet Velocity/Size and Mixture Distribution in a Single Cylinder Four Valve Spark Ignition Engine*, SAE Paper 981186.

AVL List GmbH (2004) *Engine Simulation – Physical Models*, Document No. 08.0422.0730.

AVL List GmbH (2008) *FIRE v2008 – CFD Solver*, Document No. 08.0201.0860.

Bianchi, G.M., Brusiani, F., Postrioti, L., Grimaldi, C.N., Marcacci, M. and Carmignani, L. (2007) *CFD Analysis of Injection Timing and Injector Geometry Influences on Mixture Preparation at Idle in a PFI Motorcycle Engine*, SAE Paper 2007-24-0041.

Cathcart, G., Houston, R. and Ahern, S. (2004) *The Potential of Gasoline Direct Injection for Small Displacement 4-stroke Motorcycle Applications*, SAE Paper 2004-32-0098.

Christ, A. and Schlerfer, J. (2000) 'Spray simulation for low pressure port fuel injectors', *Eighth International Conference on Liquid Atomization and Spray Systems, ICLASS-2000*, Pasadena, California, July.

Das, S. and Dent, J.C. (1995) *Simulation of the Mean Flow in the Cylinder of a Motored 4-Valved Spark Ignition Engine*, SAE Paper 952384.

Duclos, J.M. and Zolver, M. (1998) '3D modeling of intake, injection and combustion in a DI-SI engine under homogeneous and stratified operating conditions', *The Fourth International Symposium on Diagnostics and Modeling of Combustion in Internal Combustion Engines*, COMODIA 98, Kyoto, Japan.

Dukowicz, J. (1979) *Quasi-steady Droplet Change in the Presence of Convection*, Informal Report, Los Alamos Scientific Laboratory (LA7997-MS).

Gold, M.R., Arcoumanis, C., Whitelaw, J.H., Gaade, J. and Wallace, S. (2000) 'Mixture preparation strategies in an optical four-valve port-injected gasoline engine', *International Journal of Engine Research*, Vol. 1, No. 1, pp.41–56.

Gosman, A.D. (1981) *Aspects of Computer Simulation of Liquid-Fueled Combustors*, AIAA, Paper 81-0323.

Heywood, J.B. (1998) *Internal Combustion Engine Fundamental*, McGraw-Hill, New York.

Ishii, W., Hanajima, T. and Tsuzuku, H. (2004) *Application of Air-Fuel Mixture Injection to Lean-Burn engines for Small Motorcycles*, SAE Paper 2004-32-0052.

Kato, S., Hayashida, T. and Iida, M. (2007) *The Influence of Port Fuel Injection on Combustion of a Small Displacement Engine for Motorcycle*, SAE Paper 2007-32-0009.

Kim, J.H., Moon, B.S., Rhim, J.R., No, S.Y., Kim, J.Y. and Baik, S.K. (2000) 'Spray cone angles of port fuel injectors by different measuring techniques', *Eighth International Conference on Liquid Atomization and Spray Systems, ICLASS-2000*, Pasadena, California, July.

Lenz, H.P. (1992) *Mixture Formation in Spark-Ignition Engines*, Springer-Verlag/Wien, New York.

Meyer, R. and Heywood, J.B. (1997) *Liquid Fuel Transport Mechanisms into the Cylinder of a Firing Port-Injected SI Engine during Start up*, SAE Paper 970865.

Meyer, R. and Heywood, J.B. (1999) *Effect of Engine and Fuel Variables on Liquid Fuel Transport into the Cylinder in Port Injected SI Engines*, SAE Paper 1999-01-0563.

Mundo, C., Sommerfeld, M. and Tropea, C. (1998) 'On the modeling of liquid sprays impinging on surfaces', *Atomization and Sprays*, Vol. 8, pp.625–652.

Mundo, C.H.R., Sommerfeld, M. and Tropea, C. (1995) 'Droplet-wall collisions: experimental studies of the deformation and breakup process', *International Journal of Multiphase Flow*, Vol. 21, No. 2, pp.151–173.

Murakami, Y., Kurosaka, H. and Kamiya, H. (2004) *Practical Application of Combustion Simulation using CFD for Small Engine of Two-Wheeled Vehicle*, SAE Paper 2004-32-0006.

O'Rourke, P.J. and Amsden, A.A. (1987) *The TAB Method for Numerical Calculation of Spray Droplet and Breakup*, SAE Paper 872089.

Pierson, S.R., Richardson, S., Rubini, P.A., Jermy, M.C. and Greenhalgh, D.A. (2000) 'Laser characterisation of a port fuel injector to provide boundary data for computational fluid dynamics', *Intl. Conf. on Computational and Experimental Methods in Reciprocating Engines*, 1–2 November, London, UK.

Selim, M.Y.E., Dent, J.C. and Das, S. (1997) *Application of CFD to the Matching of In-Cylinder Fuel Injection and Air Motion in a Four Stroke Gasoline Engine*, SAE Paper 971601.

Shin, Y., Min, K. and Cheng, W.K. (1995) *Visualization of Mixture Preparation in a Port-fuel Injection Engine during Engine Warm-up*, SAE Paper 952481.

Wiedenhoefer, J.F. and Reitz, R.D. (2000) 'Modeling the effect of EGR and multiple injection schemes on IC engine component temperatures', *Numerical Heat Transfer: Part A: Applications*, Vol. 37, No. 7, pp.673–694.

Zhao, F.Q., Lai, M.C. and Harrington, D.L. (1995) *The Spray Characteristics of Automotive Port Fuel Injection – A Critical Review*, SAE Paper 950506.

Zhao, F.Q., Yoo, J.H. and Lai, M.C. (1996) *Spray Targeting Inside a Production-type Intake Port of a 4-valve Gasoline Engine*, SAE Paper 960115.W